

LETTER • OPEN ACCESS

Inferring dark matter substructure with astrometric lensing beyond the power spectrum

To cite this article: Siddharth Mishra-Sharma 2022 *Mach. Learn.: Sci. Technol.* **3** 01LT03

View the [article online](#) for updates and enhancements.

You may also like

- [The LHC Olympics 2020 a community challenge for anomaly detection in high energy physics](#)
Gregor Kasieczka, Benjamin Nachman, David Shih et al.
- [A Universal Power-law Prescription for Variability from Synthetic Images of Black Hole Accretion Flows](#)
Boris Georgiev, Dominic W. Pesce, Avery E. Broderick et al.
- [Characterizing and Mitigating Intraday Variability: Reconstructing Source Structure in Accreting Black Holes with mm-VLBI](#)
Avery E. Broderick, Roman Gold, Boris Georgiev et al.



LETTER

Inferring dark matter substructure with astrometric lensing beyond the power spectrum

OPEN ACCESS

RECEIVED

3 November 2021

REVISED

16 December 2021

ACCEPTED FOR PUBLICATION

7 January 2022

PUBLISHED

19 January 2022

Original Content from this work may be used under the terms of the [Creative Commons Attribution 4.0 licence](#).

Any further distribution of this work must maintain attribution to the author(s) and the title of the work, journal citation and DOI.

Siddharth Mishra-Sharma^{1,2,3,4,5} ¹ The NSF AI Institute for Artificial Intelligence and Fundamental Interactions, Cambridge, MA 02139, United States of America² Center for Theoretical Physics, Massachusetts Institute of Technology, Cambridge, MA 02139, United States of America³ Department of Physics, Massachusetts Institute of Technology, Cambridge, MA 02139, United States of America⁴ Department of Physics, Harvard University, Cambridge, MA 02138, United States of America⁵ Center for Cosmology and Particle Physics, Department of Physics, New York University, New York, NY 10003, United States of AmericaE-mail: smsharma@mit.edu**Keywords:** astrostatistics techniques (1886), cosmology (343), dark matter (353), gravitational lensing (670), convolutional neural networks (1938), astrometry (80)**Abstract**

Astrometry—the precise measurement of positions and motions of celestial objects—has emerged as a promising avenue for characterizing the dark matter population in our Galaxy. By leveraging recent advances in simulation-based inference and neural network architectures, we introduce a novel method to search for global dark matter-induced gravitational lensing signatures in astrometric datasets. Our method based on neural likelihood-ratio estimation shows significantly enhanced sensitivity to a cold dark matter population and more favorable scaling with measurement noise compared to existing approaches based on two-point correlation statistics. We demonstrate the real-world viability of our method by showing it to be robust to non-trivial modeled as well as unmodeled noise features expected in astrometric measurements. This establishes machine learning as a powerful tool for characterizing dark matter using astrometric data.

1. Introduction and background

Although there exists plenty of evidence for dark matter (DM) on galactic scales and above (see Green (2021) for a recent overview), the distribution of DM clumps—subhalos—on sub-galactic scales is less well-understood and remains an active area of cosmological study. This distribution additionally correlates with and may provide clues about the underlying particle physics nature of DM (see e.g. Bode *et al* (2001), Dalcanton and Hogan (2001), Schutz (2020)), highlighting its relevance across multiple domains.

While more massive DM subhalos can be detected and studied through their association with luminous tracers such as bound stellar populations, subhalos with smaller masses $\lesssim 10^9 M_\odot$ are not generally associated with luminous matter (Fitts *et al* 2017, Read *et al* 2017), rendering their characterization challenging. Gravitational effects provide one of the few avenues to probe the distribution of these otherwise-invisible subhalos (Buckley and Peter 2018). Gravitational lensing i.e. the bending of light from a background source due to a foreground mass, is one such effect and has been proposed in various incarnations as a probe of dark subhalos. Strong gravitational lensing, for example, has been used to infer the presence of DM substructure in galaxies outside of our own (Vegetti *et al* 2010, 2012, Hezaveh *et al* 2016, Gilman *et al* 2020). Astrometric lensing, on the other hand, has recently emerged as a promising way to characterize the DM subhalo population within the Milky Way.

Astrometry refers to the precise measurement of the positions and motions of luminous celestial objects like stars and galaxies. Gravitational lensing of these background objects by a moving foreground mass, such as a DM subhalo, can imprint a characteristic, correlated signal on their measured kinematics (angular velocities and/or accelerations). Van Tilburg *et al* (2018) introduced several methods for extracting this signature, including computing convolutions of the expected lensing signal on astrometric datasets and

detecting local kinematic outliers. Mondino *et al* (2020) applied the former method to data from the *Gaia* satellite, obtaining constraints on the abundance of dark compact objects in the Milky Way and showcasing the applicability of astrometric DM searches in a practical setting. Finally, Mishra-Sharma *et al* (2020) proposed using the angular power spectrum of the astrometric field as an observable to infer the population properties of subhalos in our Galaxy, leveraging the collective, correlated signal of a large subhalo sample.

Astrometric datasets are inherently high-dimensional, consisting of positions and kinematics of potentially millions of objects. Especially when the expected signal consists of the collective imprint of a large number of lenses, characterizing their population properties involves marginalizing over all possible configurations of subhalos, rendering the likelihood intractable and usually necessitating the use of simplified data representations like the power spectrum. While effective, such simplification can result in loss of information compared to that contained in the original dataset when the expected signal is non-Gaussian in nature. The existence of systematic effects that are degenerate with a putative signal in the low-dimensional summary domain can further inhibit sensitivity.

The dawn of the era of precision astrometry, with the *Gaia* satellite (Gaia Collaboration 2016) having recently delivered the most precise astrometric dataset to-date (Lindgren *et al* 2018, Gaia Collaboration 2018a, 2021) and surveys including the Square Kilometer Array (SKA) (Fomalont and Reid 2004, Jarvis *et al* 2015) and Roman Space Telescope (WFIRST Astrometry Working Group 2019) set to achieve further leaps in sensitivity over the next decade, calls for methods that can extract more information from these datasets than is possible using existing techniques. In this direction, Vattis *et al* (2020) proposed using a binary classifier in order to detect either the presence or absence of a substructure signal in astrometric maps. In this paper, we introduce an *inference* approach that uses spherical convolutional neural networks—exploiting the symmetry structure of the signal and data domain—in conjunction with parameterized classifiers (Cranmer *et al* 2015, Baldi *et al* 2016) in order to estimate likelihood ratios associated with the abundance of a cold DM population directly from a binned map of the astrometric velocity field. We show that our method outperforms established proposals based on the two-point correlation statistics of the astrometric field, both in absolute sensitivity as well as its scaling with measurement noise. While we focus on the specific domain application to astrometric DM searches, we note that the method as presented here is broadly applicable to data sampled on the celestial sphere, which is ubiquitous in astrophysics and cosmology. More generally, the paper showcases how neural network architectures suited to processing real-world data structures—in our cases, pixelated vector fields of velocities on the celestial sphere—can be combined with advancements in simulation-based inference in order to directly perform inference on complex, high-dimensional datasets without resorting to the use of simplified summary statistics.

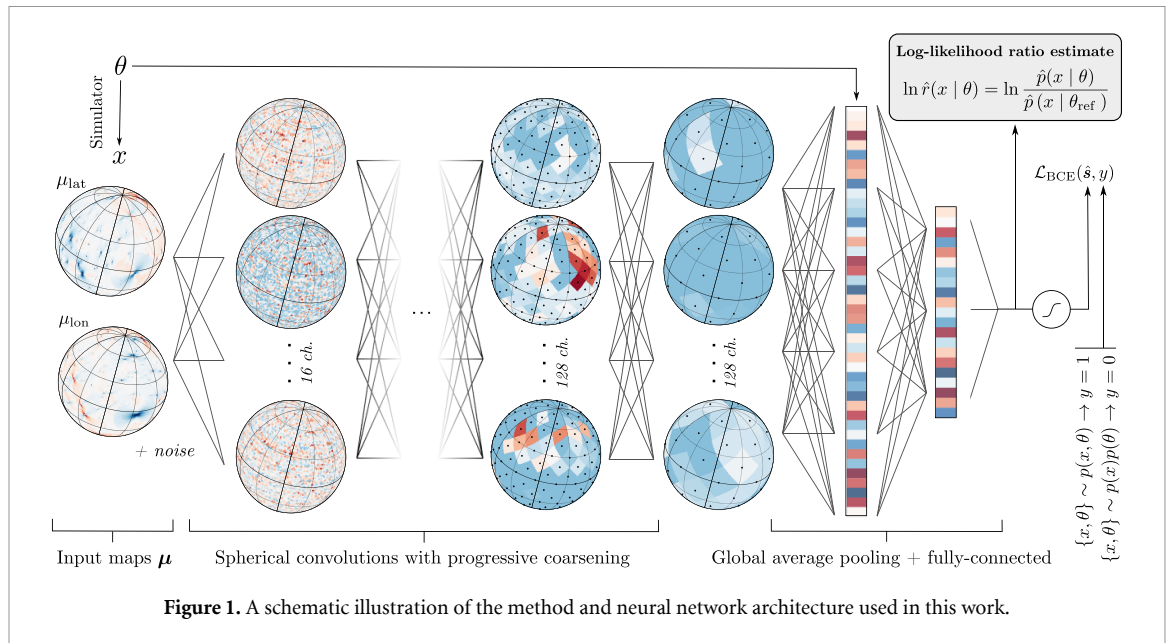
2. Model and inference

2.1. The forward model

Our datasets consist of the 2-dimensional angular velocity map of background sources on the celestial sphere. In order to define the forward model we need to specify the properties of background sources as well as the population properties of DM subhalos acting as gravitational lenses. We focus in this work on subhalos within the canonical cold DM scenario; details of the population model along with a the prescription for computing the induced velocity signal are provided in [appendix](#). The subhalo fraction $f_{\text{sub}} \in \mathbb{R}$, quantifying the expected fraction of the mass of the Milky Way contributed by subhalos in the range 10^{-6} – $10^{10} M_{\odot}$, is taken to be the parameter of interest.

We take our source population to consist of remote, point-like galaxies known as quasars which, due to their large distances from the Earth, are not expected to have significant intrinsic angular velocities. We assume the sources to be isotropically-distributed in the baseline configuration, and further study the effect of relaxing this assumption using an existing catalog of quasars from *Gaia*'s second data release (DR2). The velocity maps are assumed to be spatially binned, and we use a *HEALPix* binning (Gorski *et al* 2005) with resolution parameter $n_{\text{side}} = 64$, corresponding to $N_{\text{pix}} = 49,152$ pixels over the full sky with pixel area $\sim 0.8 \text{ deg}^2$. The values within each pixel then quantify the average latitudinal and longitudinal velocity components of quasars within that pixel. An example of the induced velocity signal on part of the celestial sphere, projected along the Galactic latitudinal and longitudinal directions and exhibiting dipole-like structures, is shown in the leftmost column of figure 1. This pixelization level was motivated by the results of Mishra-Sharma *et al* (2020), which showed the typical angular size of cold DM subhalos significantly contributing to the astrometric lensing signal to be much larger than the degree-scale pixel size used here. This can also be seen from the simulated signal realizations in figure 1.

In order to enable a comparison with traditional approaches—which are generally not expected to be sensitive to a cold DM subhalo population with next-generation astrometric surveys (Van Tilburg *et al* 2018, Mishra-Sharma *et al* 2020)—we benchmark using an optimistic observational configuration corresponding



to measuring the proper motions of $N_q = 10^8$ quasars over the fully sky with noise $\sigma_\mu = 0.1 \mu\text{as yr}^{-1}$. The final input maps $x \in \mathbb{R}^{2N_{\text{pix}}}$ are obtained by combining the simulated signal with a realization of the noise model.

2.2. The power spectrum approach

Mishra-Sharma *et al* (2020) introduced an approach for extracting the astrometric signal due to a DM subhalo population by decomposing the observed map into its angular (vector) power spectrum. The power spectrum is a summary statistic ubiquitous in astrophysics and cosmology and quantifies the amount of correlation contained at different spatial scales. In the case of data on a sphere, the basis of spherical harmonics is often used, and the power spectrum then encodes the correlation structure on different multipoles ℓ . The power spectrum effectively captures the linear component of the signal and, when the underlying signal is a Gaussian random field, captures *all* of the relevant information contained in the map(s) (Tegmark 1997). The expected signal in the power spectrum domain can be evaluated semi-analytically using the formalism described in Mishra-Sharma *et al* (2020) and, assuming a Gaussian likelihood, the expected sensitivity can be computed using a Fisher forecasting approach. We use this prescription as a comparison point to the method introduced here.

While effective, reduction of the full astrometric map to its power spectrum results in loss of information; this can be seen from the fact that the signal in the leftmost column of figure 1 is far from Gaussian. Furthermore, the existence of correlations on large angular scales due to e.g. biases in calibration of celestial reference frames (Gaia Collaboration 2018b) or systematic variations in measurements taken over different regions of the sky introduces degeneracies with a putative signal and precludes their usage in the present context. For this reason multipoles $\ell < 10$ were discarded in Mishra-Sharma *et al* (2020), degrading the projected sensitivity.

2.3. Likelihood-ratio estimation using parameterized classifiers

Recent advances in machine learning have enabled methods that can be used to efficiently perform inference on models defined through complex simulations; see Cranmer *et al* (2020) for a recent review. Here, we make use of neural likelihood-ratio estimation (Cranmer *et al* 2015, Baldi *et al* 2016, Brehmer *et al* 2018a, 2018b, 2020, Hermans *et al* 2019), previously applied to the problem of inferring DM substructure using observations of strong gravitational lenses (Brehmer *et al* 2019) and cold stellar streams (Hermans *et al* 2020).

Given a classifier that can distinguish between samples $\{x\} \sim p(x | \theta)$ drawn from parameter points θ and those from a fixed reference hypothesis $\{x\} \sim p(x | \theta_{\text{ref}})$, the decision function output by the optimal classifier $s(x, \theta) = p(x | \theta) / (p(x | \theta) + p(x | \theta_{\text{ref}}))$ is one-to-one with the likelihood ratio, $r(x | \theta) \equiv p(x | \theta) / p(x | \theta_{\text{ref}}) = s(x, \theta) / (1 - s(x, \theta))$, a fact appreciated as the likelihood-ratio trick (Cranmer *et al* 2015, Mohamed and Lakshminarayanan 2017). The classifier $s(x, \theta)$ in this case is a neural network that can work directly on the high-dimensional data, and is parameterized by the parameter of interest θ by having it included as an additional input feature. In order to improve numerical stability and reduce dependence on the fixed reference hypothesis θ_{ref} , we follow Hermans *et al* (2019) and train a classifier to

distinguish between data-sample pairs from the joint distribution $\{x, \theta\} \sim p(x, \theta)$ and those from a product of marginal distributions $\{x, \theta\} \sim p(x)p(\theta)$ (defining the reference hypothesis and in practice obtained by shuffling samples within a batch) using the binary cross-entropy (BCE) loss as the optimization objective.

We briefly highlight the advantages of this method over traditional paradigms for simulation-based inference such as Approximate Bayesian Computation (ABC, Rubin (1984), Sisson *et al* (2018)). In ABC, samples $\{x\}$ from the forward model are compared to a particular dataset x' , with the approximate posterior defined through the set of parameters whose corresponding samples most closely match the dataset of interest according to a similarity metric. In our case, the curse of dimensionality would require a manual reduction of the raw datasets $x \in \mathbb{R}^{2N_{\text{pix}}}$ into lower-dimensional summaries $f(x) \in \mathbb{R}^n$ with $n \ll 2N_{\text{pix}}$ (e.g. the power spectrum), in order to enable tractable inference. A similarity metric and tolerance threshold $\|f(x) - f(x')\| < \epsilon$ must additionally be specified in order to trade off between sample efficiency and inference precision. The machine learning-based method, on the other hand, uses neural networks in order to directly extract useful representations from high-dimensional datasets and can learn a continuous mapping from the data to the statistic of interest, in our case the likelihood ratio. Finally, ABC inference has to be performed anew for each dataset of interest. Our method, in contrast, is *amortized*—following an upfront computational cost associated with training the likelihood-ratio estimator, evaluation on a new sample can be performed almost instantaneously. This allows us to efficiently test our model and compute diagnostics such as statistical coverage over large data samples.

2.4. Extracting information from high-dimensional astrometric maps

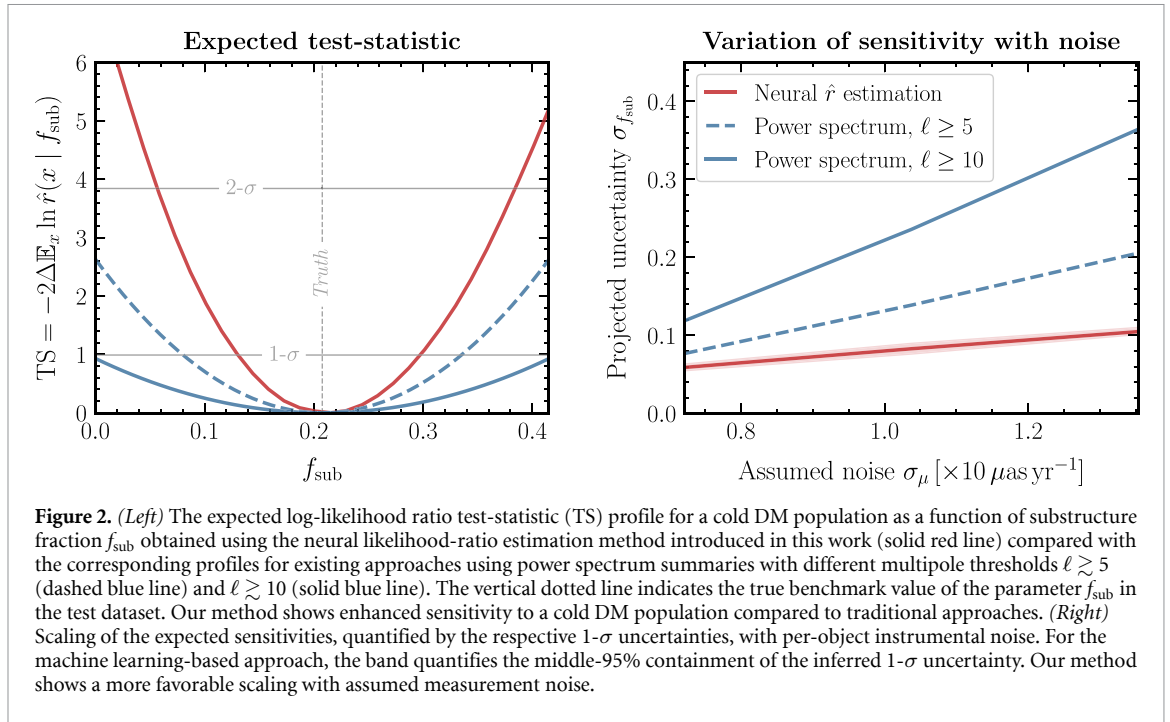
Since our data consists of a velocity field sampled on a sphere, we use a spherical convolutional neural network in order to directly learn useful representations from these maps that are efficiently suited for the downstream classification task. Specifically, we make use of *DeepSphere* (Perraudin *et al* 2019, Defferrard *et al* 2020), a graph-based convolutional neural network tailored to data sampled on a sphere. For this purpose, the *HEALPix* grid can be cast as a weighted undirected graph with N_{pix} vertices and edges connecting each pixel vertex to its set of eight neighboring pixels. The weighted adjacency matrix over neighboring pixels (i, j) is given by $A_{ij} = \exp(-\Delta r_{ij}^2 / \rho^2)$ where Δr_{ij} specifies the 3-dimensional Euclidean distance between the pixel centers and the widths ρ are obtained from Defferrard *et al* (2020). *DeepSphere* then efficiently performs convolutions in the spectral domain using a basis of Chebychev polynomials as convolutional kernels (Defferrard *et al* 2016); here, we set $K = 4$ as the maximum polynomial order.

All inputs are normalized to zero mean and unit standard deviation across the training sample. Starting with two scalar input channels representing the two orthogonal (Galactic latitude and longitude) components of the velocity vector map, we perform a graph convolution operation, increasing the channel dimension to 16 followed by a batch normalization, ReLU nonlinearity, and downsampling the representation by a factor of 4 with max pooling into the next coarser *HEALPix* resolution. Pooling leverages scale separation, preserving important characteristics of the signal across different resolutions. Four more such layers are employed, increasing the channel dimension by a factor of 2 at each step until a maximum of 128, with maps after the last convolutional layer having resolution $n_{\text{side}} = 2$ corresponding to 48 pixels. At this stage, we average over the spatial dimension (known as global average pooling (Lin *et al* 2014)) in order to encourage approximate rotation invariance, outputting 128 features onto which the parameter of interest $f_{\text{sub}} \in \mathbb{R}$ is appended. These features are passed through a fully-connected network with (1024, 128) hidden units and ReLU activations outputting the classifier decision \hat{s} by applying a sigmoidal projection.

We note that the signal in our case does not respect strict rotation invariance—as described in appendix, the motion of the Sun relative to the frame of rest of the Milky Way induces a preferred direction in the velocities of DM subhalos relative to our frame of reference, breaking the rotation symmetry of the signal. The anisotropy in the data domain is further exacerbated in the case of a realistic noise model (as explored in section 3.3 below) where measured uncertainties vary along different directions on the celestial sphere. We finally note that by representing the input angular velocity vector field in terms of two independent scalar channels, we explicitly break the rotation equivariance of spherical convolutions due to differences in how scalar and vector representations transform under rotations (see, e.g. Esteves *et al* (2020)). Given these limitations, we leave a detailed study of the equivariance properties desired of the architecture in the context of our application to future work.

2.5. Model training and evaluation

10^5 maps from the forward model were produced, with 15% of these held out for validation. Samples containing between 0 and 300 subhalos in expectation over the mass range $10^8 - 10^{10} M_{\odot}$, approximately corresponding to substructure fractions f_{sub} between 0 and 0.4, were generated from a uniform proposal distribution. The estimator was trained using a batch size of 64 for up to 50 epochs with early stopping if the validation loss had not improved after 10 epochs. The ADAM optimizer (Kingma and Ba 2017) was used with



initial learning rate 10^{-3} decayed through cosine annealing. A coarse grid search was used to inform the architecture and hyperparameter choices in this work. Experiments were performed on NVIDIA RTX8000 GPUs, taking ~ 10 min per training epoch for a total training time of $\sim 6\text{--}9$ h contingent on early stopping.

For a given test map, the log-likelihood ratio profile can be obtained by evaluating the trained estimator for different values of f_{sub} while keeping the input map fixed. The network output prior to the final sigmoidal projection directly gives the required log-likelihood ratio estimate: $\ln \hat{r} = S^{-1}(\hat{s})$, where S is the sigmoid function (Hermans *et al* 2019, 2020). Figure 1 presents an illustrative summary of the neural network architecture and method used in this work.

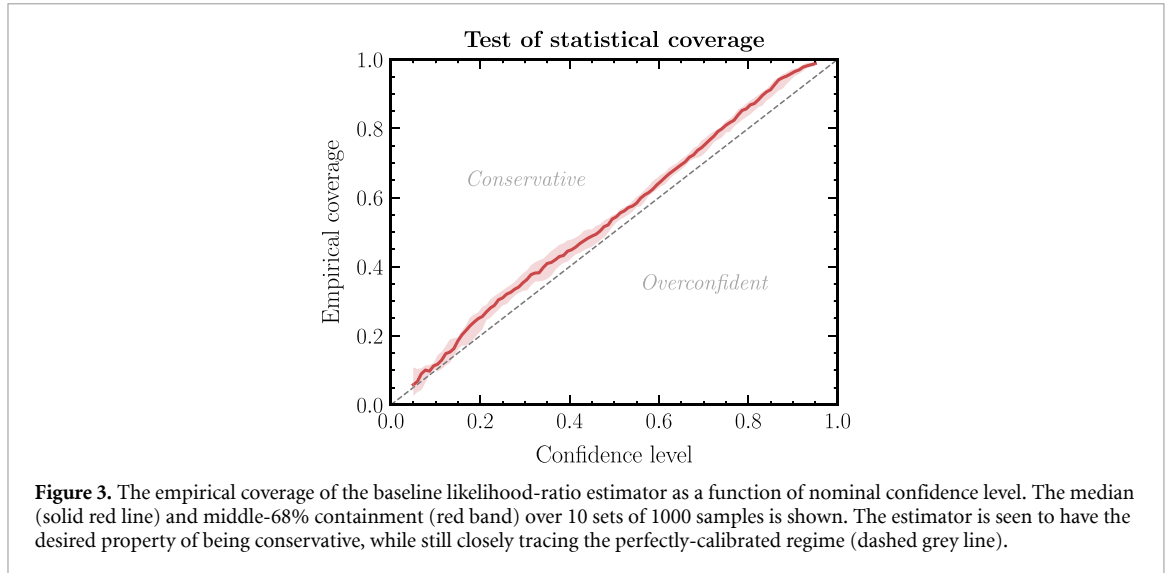
3. Experiments on simulated data

3.1. Baseline results and diagnostics

We evaluate our trained likelihood-ratio estimator on maps drawn from a benchmark configuration motivated by Springel *et al* (2008), Hütten *et al* (2016), containing 150 subhalos in expectation between 10^8 and $10^{10} M_{\odot}$ and corresponding to $f_{\text{sub}} \simeq 0.2$. The left panel of figure 2 shows the expected log-likelihood ratio test-statistic (TS) as a function of substructure fraction f_{sub} for this nominal configuration. This is obtained by evaluating the trained estimator on 100 test maps over a uniform grid in f_{sub} and taking the point-wise mean. Corresponding curves using the power spectrum approach are shown in blue, using minimum multipoles of $\ell \geq 5$ (dashed) and $\ell \geq 10$ (solid). Thresholds corresponding to 1- and $2\text{-}\sigma$ significance assuming a χ^2 -distributed TS are shown as the horizontal grey lines. We see that sensitivity gains of over a factor of ~ 2 can be expected for this particular benchmark when using the machine learning approach compared to the traditional power spectrum approach. No significant bias on the central value of the inferred DM abundance relative to the overall uncertainty scale is observed.

The right panel of figure 2 shows the scaling of expected $1\text{-}\sigma$ uncertainty on substructure fraction f_{sub} with assumed noise per quasar, keeping the number of quasars fixed (red, with the line showing the median and shaded band corresponding to the middle-95% containment of the uncertainty inferred over 50 test datasets) compared to the power spectrum approach (blue lines). A far more favorable scaling of the machine learning approach is seen compared to the power spectrum approach, suggesting that it is especially advantageous in low signal-to-noise regimes that are generally most relevant for DM searches.

Finally, we assess the quality of the approximate likelihood-ratio estimator through a test of statistical coverage. Within a hypothesis testing framework, this is necessary in order to ensure that the learned estimator is conservative over the parameter range of interest and does not produce overly confident or biased results (Hermans *et al* 2021). We obtain the estimated TS profile for 1000 simulated samples with true substructure fraction values drawn from the range $f_{\text{sub}} \in [0.1, 0.3]$. In doing so, we exclude parameter points towards the edges of our parameter space since the corresponding confidence intervals in these cases would



extend outside of the tested parameter range, as can also be inferred from the baseline analysis shown in figure 2. For nominal confidence levels in the range $1 - \alpha \in [0.05, 0.95]$ we compute the empirical coverage over the set of samples, defined as the fraction of samples whose true parameter values fall within the TS confidence interval. The confidence level for a given nominal confidence interval is computed under the assumption that the TS is χ^2 -distributed (Wilks 1938). The procedure is repeated for 10 different sets of 1000 samples in order to estimate the statistical uncertainty associated with the empirical coverage.

The results of the coverage test are shown in figure 3, illustrating the median (solid red line) and middle-68% containment (red band) of the empirical coverage. We see that the empirical coverage has the desired property of being conservative while still being close to the perfectly-calibrated regime (dashed grey line). We emphasize that this diagnostic tests the quality of the likelihood-ratio estimator over the entire evaluation parameter range $f_{\text{sub}} \in [0.1, 0.3]$ rather than the baseline value $f_{\text{sub}} \simeq 0.2$ in isolation.

3.2. Experiments with unmodeled noise correlated on large scales

Since the existence of measurement noise correlated on large spatial scales is a potential source of systematic uncertainty when working with astrometric maps, we test the susceptibility of our method to such effects by creating simulated data containing large-scale noise not previously seen by the trained estimator. Instead of assuming a scale-invariant noise power spectrum $C_\ell^{\text{noise}} = 4\pi\sigma_\mu^2/N_q$ (Mishra-Sharma *et al* 2020), in this case we model noise with an order of magnitude excess in power on scales $\ell \lesssim 10$, parameterized as $C_\ell^{\text{noise}} = 4\pi\sigma_\mu^2/N_q \cdot (10 - 9S(\ell - 10))$ where S denotes the sigmoid function. The left panel of figure 4 illustrates this noise model (thicker green line) as well as the power spectrum of one simulated realization from this model (thinner green line, obtained using the *HEALPix* module *anafast*) contrasted with the standard scale-invariant noise case (red lines). The right panel of figure 4 shows the expected log-likelihood ratio test-statistic profile for the two cases. Although a bias in the maximum-likelihood estimate of f_{sub} is seen when the test data has unmodeled noise (green line), the true test parameter value (dashed vertical line) is seen to lie well within the inferred 1- σ confidence interval. This suggests that the method is only marginally susceptible to substantive amounts of correlated noise on large spatial scales.

3.3. Experiments with a data-driven noise model

We finally assess the performance of our method using a realistic noise model obtained from the astrometric catalog of quasars in *Gaia*'s Data Release 2 (DR2) (Lindegren *et al* 2018, Gaia Collaboration 2018a). The catalog contains the measured 2-dimensional positions, proper motions, as well as proper motion uncertainties of 555,934 quasars. Although the measured uncertainties in this case are too large for the catalog to be viable for the current scientific use-case, they can be rescaled and used to construct a data-driven noise model for testing the viability of our method on forthcoming astrometric data.

We compute the pixel-wise proper motion uncertainties as the inverse-variance weighted values within each *HEALPix* pixel; $\sigma_\mu^{\text{pix}} = \left(\sum_{q \in \text{pix}} \sigma_{\mu,q}^{-2} \right)^{-1/2}$, where $\sigma_{\mu,q}^2$ are the provided variances of individual quasars within a given pixel. This results in a highly anisotropic noise model, shown in the left column of figure 5, additionally having different uncertainties in the latitudinal (top row) and longitudinal (bottom row) directions. As expected due to occlusion from the Galactic disk, uncertainties are significantly higher towards

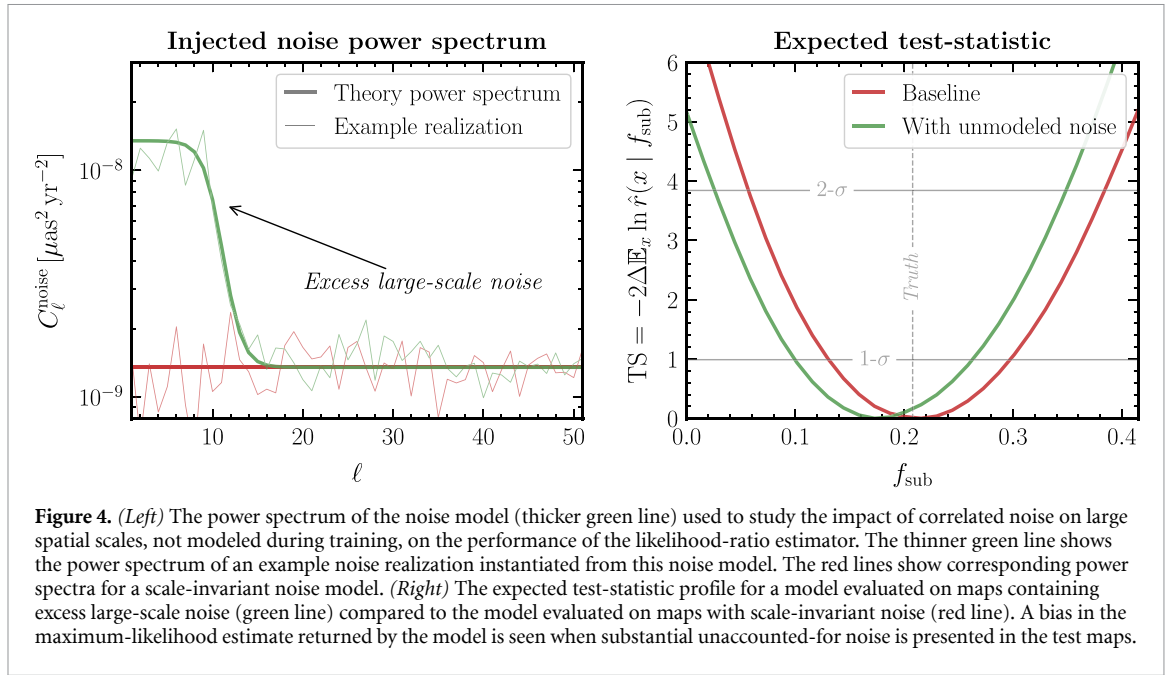


Figure 4. (Left) The power spectrum of the noise model (thicker green line) used to study the impact of correlated noise on large spatial scales, not modeled during training, on the performance of the likelihood-ratio estimator. The thinner green line shows the power spectrum of an example noise realization instantiated from this noise model. The red lines show corresponding power spectra for a scale-invariant noise model. (Right) The expected test-statistic profile for a model evaluated on maps containing excess large-scale noise (green line) compared to the model evaluated on maps with scale-invariant noise (red line). A bias in the maximum-likelihood estimate returned by the model is seen when substantial unaccounted-for noise is presented in the test maps.

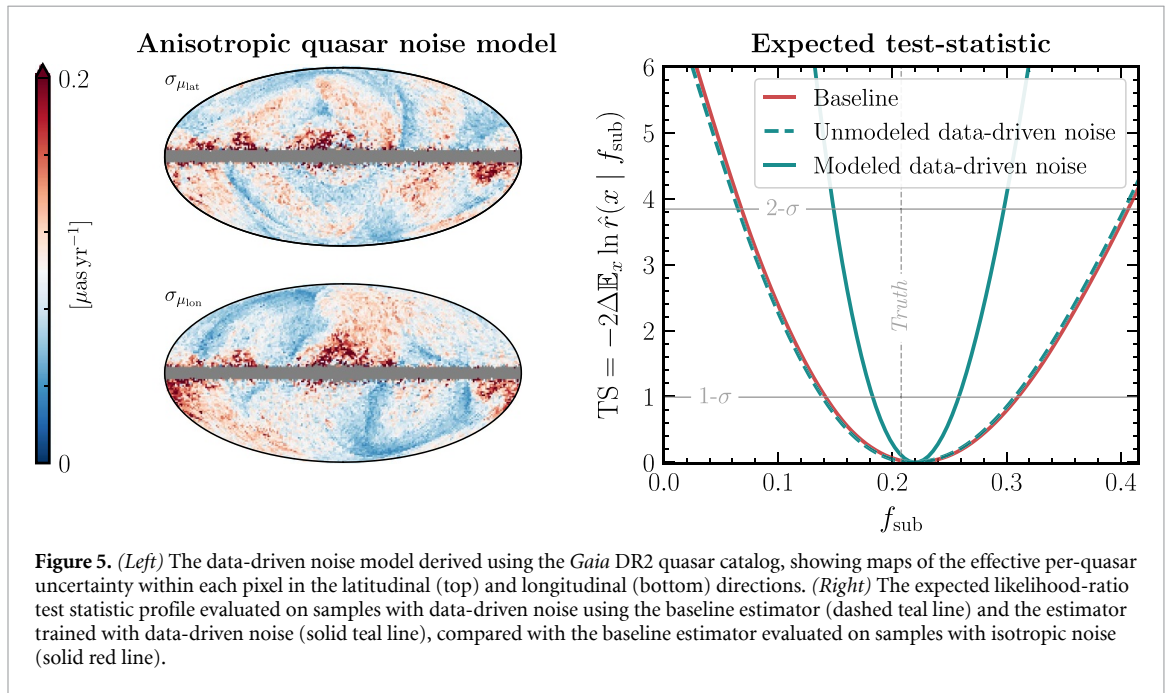


Figure 5. (Left) The data-driven noise model derived using the *Gaia* DR2 quasar catalog, showing maps of the effective per-quasar uncertainty within each pixel in the latitudinal (top) and longitudinal (bottom) directions. (Right) The expected likelihood-ratio test statistic profile evaluated on samples with data-driven noise using the baseline estimator (dashed teal line) and the estimator trained with data-driven noise (solid teal line), compared with the baseline estimator evaluated on samples with isotropic noise (solid red line).

the Galactic plane where the catalog has low completeness, additionally varying over the sky due to the scanning pattern and time-dependent instrumental response of the satellite. The region closest to the plane where no quasars are included in the catalog (shown in grey) is masked, testing the effect of partial sky coverage. In order to enable a direct comparison, the mean per-pixel variance for the data-driven noise model is normalized to that used in the baseline experiments in section 3.1.

We evaluate the expected likelihood-ratio test statistic on samples generated with the data-driven noise model using two different estimators: (a) the baseline estimator trained using samples with isotropic noise, as describe in section 3.1, and (b) an estimator trained on samples generated with the correct, data-driven noise model used during evaluation. For (b), a larger training batch size of 512 was found to provide better results, with all other hyperparameters being the same as the baseline case. The expected likelihood-ratio test statistic profiles for these cases are shown in the right column of figure 5. Interestingly, evaluating the baseline estimator on samples with the data-driven noise model (dashed teal) produces results very similar to the baseline case (solid red). Using the correct, data-driven noise model on the other hand produces tighter constraints (solid teal) due to the fact that large portions of the sky in this case have smaller modeled uncertainties compared to the baseline case. In either case, successful recover of the astrometric lensing signal

can be seen. These experiments demonstrate the viability of our method in the context of real-world applications, and we leave a more detailed study of our method in the context of forthcoming astrometric surveys and datasets to future work.

4. Conclusions and outlook

We have introduced a method to analyze astrometric datasets over large regions of the sky using techniques based on machine learning with the aim of inferring the lensing signature of a DM substructure. We have shown our method to be significantly more sensitive to a cold DM subhalo population compared to established methods based on global summary statistics, with more favorable scaling as a function of measurement noise. Since the collection and reduction of astrometric data is an expensive endeavor, the use of methods that can take advantage of more of the available information can be equated to long periods of data-taking, underscoring their importance. Additionally, unlike the power spectrum approach, the current method does not require the construction of a numerically-expensive estimator to account for non-uniform exposure, selection effects, and instrumental noise in realistic datasets. These, as well as any other modeled observational effects, can be incorporated directly at the level of the forward model.

We have focused in this work on assessing sensitivity to a cold DM-like subhalo population with quasar velocity astrometry, which is within the scope of upcoming radio surveys like the SKA (Fomalont and Reid 2004, Jarvis *et al* 2015). Our method can also be applied in a straightforward manner to look for the *acceleration* lensing signal imprinted on Milky Way stars, in particular sourced by a population of more compact subhalos than those expected in the cold DM scenario. These features are expected to imprint a larger degree of non-Gaussianity compared to the signal explored here (as can be seen, e.g. from figure 1 of Mishra-Sharma *et al* (2020)), and machine learning methods may provide larger relative sensitivity gains when deployed in that context. Such analyses are within purview of the upcoming Roman exoplanet microlensing survey (Pardo and Doré 2021) as well as future *Gaia* data releases. We note that when the region of interest covers a smaller fraction of the celestial sphere, as expected for the Roman microlensing survey of the Galactic bulge, the use of conventional convolutional architectures may be preferred as more efficient compared to spherical convolutions when the flat-sky approximation is valid.

Several improvements and extensions to the method presented in this paper are possible. The use of architectures that can equivariantly handle vector inputs (Esteves *et al* 2020) may aid in learning more efficient representations of the astrometric map. Using convolutions based on fixed rather than learned filters can additionally reduce model complexity and produce more interpretable representations (Cheng *et al* 2020, Ha *et al* 2021, McEwen *et al* 2021, Saydjari and Finkbeiner 2021, Valogiannis and Dvorkin 2021). The use of methods for likelihood-ratio estimation that can leverage additional latent information in the forward model can significantly enhance the sample efficiency of the analysis (Stoye *et al* 2018, Brehmer *et al* 2018a, 2018b, 2020). We leave the study of these extensions as well as application of our method to other DM population scenarios to future work.

Astrometric lensing has been established as a promising way to characterize the Galactic DM population, with theoretical progress in recent years going in step with advances on the observational front. While this work is a first attempt at bringing principled machine learning techniques to this field, with the availability of increasingly complex datasets we expect machine learning to be an important general-purpose tool for future astrometric DM searches.

Data availability statement

The data that support the findings of this study are openly available at the following URL/DOI: <https://github.com/smsharma/neural-global-astrometry>.

Acknowledgments

SM warmly thanks Kyle Cranmer, Cristina Mondino, Tess Smidt, Ken Van Tilburg, and Neal Weiner for helpful conversations. SM benefitted from the hospitality of the Center for Computational Astrophysics at the Flatiron Institute while this work was being performed. This work was performed in part at the Aspen Center for Physics, which is supported by National Science Foundation Grant PHY-1607611. The participation of SM at the Aspen Center for Physics was supported by the Simons Foundation. This work is supported by the NSF CAREER Grant PHY-1554858, NSF Grants PHY-1620727 and PHY-1915409, and the Simons Foundation. This work is supported by the National Science Foundation under Cooperative Agreement PHY-2019786 (The NSF AI Institute for Artificial Intelligence and Fundamental Interactions,

<http://iaifi.org/>). This material is based upon work supported by the U.S. Department of Energy, Office of Science, Office of High Energy Physics of U.S. Department of Energy under grant Contract Number DE-SC0012567. This work made use of the NYU IT High Performance Computing resources, services, and staff expertise. This research has made use of NASA's Astrophysics Data System. This work has made use of data from the European Space Agency (ESA) mission *Gaia* (<https://www.cosmos.esa.int/gaia>), processed by the *Gaia* Data Processing and Analysis Consortium (DPAC, <https://www.cosmos.esa.int/web/gaia/dpac/consortium>). Funding for the DPAC has been provided by national institutions, in particular the institutions participating in the *Gaia* Multilateral Agreement. We acknowledge the use of the *DeepSphere* graph convolutional layer implementation as well as code used to produce elements of figure 1 from the code repository associated with Defferrard *et al* (2020)⁶.

Software

Astropy (Robitaille *et al* 2013, Price-Whelan *et al* 2018), *healpy* (Gorski *et al* 2005, Zonca *et al* 2019), *IPython* (Pérez and Granger 2007), *Jupyter* (Kluyver *et al* 2016), *Matplotlib* (Hunter 2007), *MLflow* (Chen *et al* 2020), *NumPy* (Harris *et al* 2020), *PyGSP* (Defferrard *et al* 2017), *PyTorch* (Paszke *et al* 2019), *PyTorch Geometric* (Fey and Lenssen 2019), *PyTorch Lightning* (Falcon *et al* 2020), *sbi* (Tejero-Cantero *et al* 2020), *SciPy* (Virtanen *et al* 2020), and *seaborn* (Waskom *et al* 2017).

Appendix. Additional details on the forward model

We consider a population of Navarro-Frenk-White (NFW) (Navarro *et al* 1996) subhalos following a power-law mass function, $dn/dm \propto m^\alpha$, with slope $\alpha = -1.9$ as expected if the population is sourced from nearly scale-invariant primordial fluctuations in the canonical Λ Cold Dark Matter (Λ CDM) scenario. The concentration-mass relation from Sánchez-Conde and Prada (2014) is used to model the concentrations associated with density profiles of individual subhalos. Subhalos between 10^7 – $10^{10} M_\odot$ are simulated, assuming the influence of lighter subhalos to be too small to be discernable (Mishra-Sharma *et al* 2020).

The spatial distribution of subhalos in the Galactocentric frame is modeled using results from the Aquarius simulation following Springel *et al* (2008), Hütten *et al* (2016). Since this spatial distribution accounts for the depletion of subhalos towards the Galactic Center due to gravitational tidal effects, the angular number density of subhalos looking out from the Sun frame can be considered to be effectively isotropic.

The asymptotic velocities of subhalos in the Galactocentric frame are taken to follow a truncated Maxwell-Boltzmann distribution (Chandrasekhar 1939, Lisanti 2017) $f_{\text{Gal}}(\mathbf{v}) \propto e^{-v^2/v_0^2} \cdot H(v_{\text{esc}} - |\mathbf{v}|)$, where $v_{\text{esc}} = 550 \text{ km s}^{-1}$ is the Galactic escape velocity (Piffl *et al* 2014), $v_0 = 220 \text{ km s}^{-1}$ (Kerr and Lynden-Bell 1986), and H is the Heaviside step function. Once instantiated, the positions and velocities of subhalos are transformed into the Galactic frame, assuming $R_\odot = 8.2 \text{ kpc}$ to be the distance of the Sun from the Galactic Center (Gravity Collaboration 2019, Boyv 2020) and $\mathbf{v}_\odot = (11, 232, 7) \text{ km s}^{-1}$ its Galactocentric velocity (Schönrich *et al* 2010). Note that the asymmetry in the direction of motion of the Sun in the Milky Way introduces a preferred direction for the Sun-frame velocities of subhalos, breaking strict rotation invariance in the forward model. Although not explicitly pursued here, the expected characteristic form of this asymmetry can be used as an additional distinguishing handle for the lensing signal, as was done in Mishra-Sharma *et al* (2020).

Once a subhalo population has been instantiated using the forward model, the induced velocity lensing signal at different positions on the celestial sphere can be computed. Given a spherically-symmetric subhalo lens moving with transverse velocity \mathbf{v}_l , the expected lens-induced velocity for a background source at impact parameter \mathbf{b} is given by (Van Tilburg *et al* 2018)

$$\boldsymbol{\mu}(\mathbf{b}) = 4G_N \left\{ \frac{M(b)}{b^2} \left[2\hat{\mathbf{b}} \left(\hat{\mathbf{b}} \cdot \mathbf{v}_l \right) - \mathbf{v}_l \right] - \frac{M'(b)}{b} \hat{\mathbf{b}} \left(\hat{\mathbf{b}} \cdot \mathbf{v}_l \right) \right\} \quad (\text{A1})$$

where $M(b)$ and $M'(b)$ are the projected mass of the subhalo at a given impact parameter distance $b = |\mathbf{b}|$ and its gradient. In the context of our spatially-binned velocity map, \mathbf{b} represents the vector from the center of the subhalo to the center of the respective *HEALPix* pixel.

⁶ <https://github.com/deepsphere/deepsphere-pytorch>.

ORCID iD

Siddharth Mishra-Sharma  <https://orcid.org/0000-0001-9088-7845>

References

- Baldi P, Cranmer K, Faucett T, Sadowski P and Whiteson D 2016 *Eur. Phys. J. C* **76** 235
- Bode P, Ostriker J P and Turok N 2001 *Astrophys. J.* **556** 93
- Bovy J 2020 (arXiv:2012.02169)
- Brehmer J, Cranmer K, Louppe G and Pavez J 2018a *Phys. Rev. D* **98** 052004
- Brehmer J, Cranmer K, Louppe G and Pavez J 2018b *Phys. Rev. Lett.* **121** 111801
- Brehmer J, Louppe G, Pavez J and Cranmer K 2020 *Proc. Natl Acad. Sci.* **117** 5242
- Brehmer J, Mishra-Sharma S, Hermans J, Louppe G and Cranmer K 2019 *Astrophys. J.* **886** 49
- Buckley M R and Peter A H G 2018 *Phys. Rept.* **761** 1
- Chandrasekhar S 1939 An introduction to the study of stellar structure
- Chen A *et al* 2020 *Proc. of the Fourth Int. Workshop on Data Management for End-to-End Machine Learning* pp 1–4
- Cheng S, Ting Y-S, Ménard B and Bruna J 2020 *Mon. Not. Roy. Astron. Soc.* **499** 5902
- Collaboration G 2016 *Astron. Astrophys.* **595** A1
- Collaboration G 2018a *Astron. Astrophys.* **616** A1
- Collaboration G 2018b *Astron. Astrophys.* **616** A14
- Collaboration G 2019 *Astron. Astrophys.* **625** L10
- Collaboration G 2021 *Astron. Astrophys.* **649** A1
- Cranmer K, Brehmer J and Louppe G 2020 *Proc. Natl Acad. Sci.* **117** 30055
- Cranmer K, Pavez J and Louppe G 2015 (arXiv:1506.02169)
- Dalcanton J J and Hogan C J 2001 *Astrophys. J.* **561** 35
- Defferrard M, Bresson X and Vandergheynst P 2016 (arXiv:1606.09375)
- Defferrard M, Martin L, Pena R and Perraudin N 2017 PyGSP: Graph Signal Processing in Python, v0.5.0 Zenodo (available at: <https://doi.org/10.5281/zenodo.1003158>)
- Defferrard M, Milani M, Gusset F and Perraudin N 2020 (arXiv:2012.15000)
- Esteves C, Makadia A, Daniilidis K, Larochelle H *et al* 2020 *Advances in Neural Information Processing Systems 33: Conf. on Neural Information Processing Systems 2020, NeurIPS, December 6–12, 2020, Virtual ed Larochelle H et al*
- Falcon W *et al* 2020 PyTorchLightning/pytorch-lightning: 0.7.6 release, 0.7.6 Zenodo
- Fey M and Lenssen J E 2019 *ICLR Workshop on Representation Learning on Graphs and Manifolds*
- Fitts A *et al* 2017 *Mon. Not. Roy. Astron. Soc.* **471** 3547
- Fomalont E B and Reid M 2004 *New Astron. Rev.* **48** 1473
- Gilman D, Birrer S and Nierenberg A *et al* 2020 *Mon. Not. Roy. Astron. Soc.* **491** 6077
- Gorski K M, Hivon E and Banday A J *et al* 2005 *Astrophys. J.* **622** 759
- Green A M 2021 *Les Houches Summer School on Dark Matter*
- Ha W, Singh C, Lanusse F, Upadhyayula S and Yu B 2021 (arXiv:2107.09145)
- Harris C R *et al* 2020 *Nature* **585** 357
- Hermans J, Banik N, Weniger C, Bertone G and Louppe G 2020 (arXiv:2011.14923)
- Hermans J, Begy V and Louppe G 2019 (arXiv:1903.04057)
- Hermans J, Delaunoy A, Rozet F, Wehenkel A and Louppe G 2021 Averting a crisis in simulation-based inference (arXiv:2110.06581)
- Hezaveh Y D *et al* 2016 *Astrophys. J.* **823** 37
- Hunter J D 2007 *Comput. Sci. Eng.* **9** 90
- Hütten M, Combet C, Maier G and Maurin D 2016 *JCAP* **09** 047
- Jarvis M J *et al* 2015 (arXiv:1501.03825)
- Kerr F J and Lynden-Bell D 1986 *Mon. Not. Roy. Astron. Soc.* **221** 1023
- Kingma D P and Ba J 2017 Adam: a method for stochastic optimization (arXiv:1412.6980)
- Kluyver T *et al* 2016 ELPUB
- Lin M, Chen Q and Yan S 2014 Network in network (arXiv:1312.4400)
- Lindgren L, Hernández J and Bombrun A *et al* 2018 *A & A* **616** A2
- Lisanti M 2017 *Theoretical Advanced Study Institute in Elementary Particle Physics: New Frontiers in Fields and Strings* (Singapore: World Scientific) pp 399–446
- McEwen J D, Wallis C G R and Mavor-Parker A N 2021 (arXiv:2102.02828)
- Mishra-Sharma S, Van Tilburg K and Weiner N 2020 *Phys. Rev. D* **102** 023026
- Mohamed S and Lakshminarayanan B 2017 Learning in implicit generative models (arXiv:1610.03483)
- Mondino C, Taki A-M, Van Tilburg K and Weiner N 2020 *Phys. Rev. Lett.* **125** 111101
- Navarro J F, Frenk C S and White S D M 1996 *Astrophys. J.* **462** 563
- Pardo K and Doré O 2021 (arXiv:2108.10886)
- Paszke A *et al* 2019 *Advances in Neural Information Processing Systems 32* (Red Hook, NY: Curran Associates, Inc.) pp 8024–35
- Pérez F and Granger B E 2007 *Comput. Sci. Eng.* **9** 21
- Perraudin N, Defferrard M, Kacprzak T and Sgier R 2019 *Astron. Comput.* **27** 130
- Piffi T *et al* 2014 *Astron. Astrophys.* **562** A91
- Price-Whelan A *et al* 2018 *Astron. J.* **156** 123
- Read J I, Iorio G, Agertz O and Fraternali F 2017 *Mon. Not. Roy. Astron. Soc.* **467** 2019
- Robitaille T P *et al* 2013 *Astron. Astrophys.* **558** A33
- Rubin D B 1984 *Ann. Statist.* **12** 1151
- Sánchez-Conde M A and Prada F 2014 *Mon. Not. Roy. Astron. Soc.* **442** 2271
- Saydjari A K, and Finkbeiner D P 2021 (arXiv:2104.11244)
- Schönrich R, Binney J and Dehnen W 2010 *Mon. Not. Roy. Astron. Soc.* **403** 1829
- Schutz K 2020 *Phys. Rev. D* **101** 123026

- Sisson S A, Fan Y and Beaumont M 2018 *Handbook of Approximate Bayesian Computation* (Boca Raton, FL: CRC Press)
- Springel V, Wang J and Vogelsberger M *et al* 2008 *Mon. Not. Roy. Astron. Soc.* **391** 1685
- Stoye M, Brehmer J, Louppe G, Pavez J and Cranmer K 2018 (arXiv:1808.00973)
- Tegmark M 1997 *Phys. Rev. D* **55** 5895
- Tejero-Cantero A *et al* 2020 *J. Open Source Softw.* **5** 2505
- Valogiannis G and Dvorkin C 2021 (arXiv:2108.07821)
- Van Tilburg K, Taki A-M and Weiner N 2018 *J. Cosmol. Astropart. Phys.* **07** 041
- Vattis K, Toomey M W and Koushiappas S M 2020 (arXiv:2008.11577)
- Vegetti S, Koopmans L V E, Bolton A, Treu T and Gavazzi R 2010 *Mon. Not. Roy. Astron. Soc.* **408** 1969
- Vegetti S, Lagattuta D J and McKean J P *et al* 2012 *Nature* **481** 341
- Virtanen P *et al* 2020 *Nat. Methods* **17** 261
- Waskom M *et al* 2017 mwaskom/seaborn: v0.8.1 (September 2017), v0.8.1 Zenodo (available at: <https://doi.org/10.5281/zenodo.883859>)
- WFIRST Astrometry Working Group 2019 *J. Astron. Telescopes Instrum. Syst.* **5** 044005
- Wilks S S 1938 *Ann. Math. Stat.* **9** 60
- Zonca A, Singer L and Lenz D *et al* 2019 *J. Open Source Softw.* **4** 1298